AIAA Journal
Vol. 52, No. 9, September 2014

Modeling of Broadband Moving Sources for Time-Domain Simulations of Outdoor Sound Propagation

Didier Dragna* and Philippe Blanc-Benon†
École Centrale de Lyon, 69134 Écully Cedex, France
and
Franck Poisson‡
SNCF, 75611 Paris Cedex 12, France

DOI: 10.2514/1.J052672

Although time-domain solutions of the linearized Euler equations are well adapted to study the acoustic propagation in an outdoor environment, the modeling of sources in motion in time-domain solvers has not been investigated in the literature yet. This is done here by considering distributed volume sources. First, the influence of the spatial distribution of the source on the acoustic field is analyzed. Results obtained for a nonmoving source are summarized, and the example of a Gaussian spatial distribution is presented. The case of a harmonic volume source moving at a constant speed is then investigated in the geometrical far field. The directivity of a noncompact source is shown to be dramatically different from that of a point source. Numerical simulations are performed in a three-dimensional geometry in free-field configurations, and waveforms of the acoustic pressure exhibit Doppler shift and convective amplification. Finally, simulations of a broadband moving source above an impedance ground surface are presented. For a rigid ground, strong destructive and constructive interferences are observed. The numerical solution is in a very good agreement with an analytical solution. For finite-impedance surfaces, interferences are smoothed, and the acoustic pressure strongly depends on the impedance model. A low-frequency contribution is observed close to the ground in accordance with the ground characteristics.

Nomenclature

B = characteristic length scale of the spatial distribution of the source, m
c_0 = sound speed, $\mathrm{m \cdot s^{-1}}$
f = frequency, Hz
f_0 = frequency of a harmonic source, Hz
k = wave number, $\mathrm{m^{-1}}$
M_0 = Mach number
$\boldsymbol{M}_0$ = Mach number vector
p = acoustic pressure, Pa
Q = spatial distribution of the source, $\mathrm{s^{-1}}$
$\hat{Q}$ = Fourier transform of the spatial distribution of the source, $\mathrm{m^3 \cdot s^{-1}}$
$\boldsymbol{R}$ = vector between the observation point and the position of the source, m
S = source term, $\mathrm{s^{-1}}$
S_0 = normalization factor for the source term, $\mathrm{m^3 \cdot s^{-1}}$
s = source signal
t = time, s
V_0 = source speed, $\mathrm{m \cdot s^{-1}}$
$\boldsymbol{V}_0$ = source speed vector, $\mathrm{m \cdot s^{-1}}$
$\boldsymbol{v}$ = acoustic velocity vector, $\mathrm{m \cdot s^{-1}}$
δ = Dirac delta function
θ = angle between vectors $\boldsymbol{R}$ and $\boldsymbol{V}_0$, rad
λ = wavelength, m
ρ_0 = mean density of the medium, $\mathrm{kg \cdot m^{-3}}$
σ = airflow resistivity, $\mathrm{Pa \cdot s \cdot m^{-2}}$
ϕ = acoustic potential, $\mathrm{m^2 \cdot s^{-1}}$
ω = angular frequency, $\mathrm{rad \cdot s^{-1}}$
ω_0 = angular frequency of a harmonic source, $\mathrm{rad \cdot s^{-1}}$

Subscript

e = quantity evaluated at the emission time

I. Introduction

IN TRANSPORTATION noise applications, many complex phenomena impacting sound propagation must be taken into account. Time-domain methods are well suited to deal with these aspects and have become a reference tool for more than 10 years. Many studies have been conducted to account for meteorological conditions [1], effects of surface impedances [2,3], and topography [4,5]. Among the remaining issues is the modeling of realistic sources and in particular of moving sources. In current applications, acoustic sources are often described as a sum of simpler equivalent sources. For instance, in the context of railway noise, the train is described in most of the existing prediction tools by a line source or by a set of point sources. The use of Green's functions is limited to very simple configurations and is unpractical for realistic scenarios in which wind profiles and topography must be accounted for. Engineering models based on analytical calculations [6] or simplified numerical models, such as ray tracing or two-dimensional (2-D) parabolic equation computations, have then been proposed to treat long-range sound propagation [7]. These approaches can be validated using reference time-domain methods.

Although implementation of moving sources in time-domain solvers has been discussed previously [8], this has not been done yet in the literature, as far as we know. One of the main reasons is that simple acoustic sources as point sources are generally spatial singularities, which is problematic for their implementation in time-domain solvers. Indeed, because they are spatial singularities, the source must be set on a grid node at each iteration. Thus, for a given trajectory, the grid must be generated with that constraint in mind.

Presented as Paper 2012-2109 at the 18th AIAA/CEAS Aeroacoustics Conference, Colorado Springs, CO, 4–6 June 2012; received 5 April 2013; revision received 27 November 2013; accepted for publication 6 December 2013; published online 21 April 2014.

*Assistant Professor, Laboratoire de Mécanique des Fluides et d'Acoustique, UMR CNRS 5509, Université de Lyon; didier.dragna@ec-lyon.fr.

†Senior Research Scientist, Laboratoire de Mécanique des Fluides et d'Acoustique, UMR CNRS 5509, Université de Lyon; philippe.blanc-benon@ec-lyon.fr. Member AIAA.

‡Research Engineer, Direction de l'Innovation et de la Recherche; franck.poisson@sncf.fr.

Moreover, even in the simplest case of a source moving at a constant speed V_0, it is not straightforward to account for a point source. Indeed, in explicit time-marching methods, the Courant–Friedrichs–Lewy (CFL) number, defined by CFL $= c_0\Delta t/\Delta x$ where Δx and Δt are, respectively, the spatial and time steps and where c_0 is the sound speed, must remain small to avoid numerical instabilities. During one time step, the source moves at least to one spatial step. Thus, the source Mach number $M = V_0/c_0$ satisfies the relation $M = 1/\mathrm{CFL}$, which shows that the Mach number must not be too small to ensure stability. This leads to a severe restriction on the source speed for practical applications. This problem can be handled using interpolation of the acoustic field at each time step so that the point source can be located on a grid node. This would, however, require a large computational effort.

In this paper, distributed volume sources are used to avoid these issues. For a nonmoving source, it is known [9,10] that the spatial distribution modifies the acoustic field obtained for a point source by modulating the amplitude by the Fourier transform of the volume source distribution. For a moving source, it is also expected that the Fourier transform plays a role. Note that in this study we consider only distributed volume sources and not the case of rigid bodies in motion as done for instance in [11]. The main objective of the paper is to show that time-domain solvers are well suited to deal with moving sources. In particular, they allow one to consider acoustic radiation of moving sources above impedance surfaces, which remains an open and complex problem, as analytical solutions have been obtained only in the case of a frequency-independent surface impedance [12].

The paper is organized as follows. In Sec. II, the effects of a volume source distribution on the acoustic field are studied. First, the analytical solution for a harmonic source obtained with a geometrical far-field approximation is summarized. The example of a Gaussian spatial distribution is developed to examine the validity of the approximation. Then, the case of a harmonic source moving at a constant speed is considered and a geometrical far-field approximation is performed to highlight the influence of the spatial distribution. Results obtained with a solver of the linearized Euler equations for a three-dimensional (3-D) geometry are compared with those obtained with the derived analytical solution for a spherical source and for a finite-length line source. In Sec. III, numerical simulations of a broadband source moving above an impedance ground surface are presented. Sound pressure levels (SPLs) obtained in the case of a rigid ground are compared with those obtained for a ground surface of finite impedance.

II. Effects of the Source Distribution on the Acoustic Field in Simple Cases

Effects of the source distribution on the acoustic field are studied in the free field in the absence of mean flow in the cases of a nonmoving source and of a source moving at a constant speed. To do so, we consider the acoustic potential ϕ such as $p = -\rho_0\partial\phi/\partial t$ and $\boldsymbol{v} = \nabla\phi$, where p and $\boldsymbol{v}$ denote the acoustic pressure and the acoustic velocity, respectively. The term ρ_0 is the mean air density. This potential satisfies the inhomogeneous Helmholtz equation:

$$\frac{1}{c_0^2}\frac{\partial^2\phi}{\partial t^2} - \Delta\phi = S(\mathbf{x}(t), t) \tag{1}$$

where t denotes the time and S is the source term. The origin of the coordinates system is the center of the source. The general solution of Eq. (1) is (see, e.g., [13])

$$\phi(\mathbf{x}, t) = \frac{1}{4\pi}\int_{-\infty}^{+\infty}\int_V S(\mathbf{y}(t'), t')\delta\left(t' - t + \frac{r}{c_0}\right)\frac{\mathrm{d}\mathbf{y}\,\mathrm{d}t'}{r} \tag{2}$$

where V denotes the entire space and with $r = |\mathbf{x} - \mathbf{y}|$.

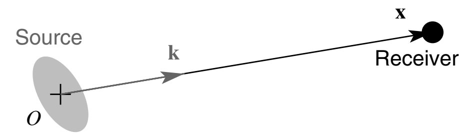

Fig. 1 Nonmoving volume source in the free field.

A. Nonmoving Sources

1. Analytical Expression for a Harmonic Source in the Geometrical Far Field

In this section, a harmonic nonmoving source is considered, with a source term:

$$S(\mathbf{x}, t) = Q(\mathbf{x})\exp(-i\omega_0 t) \tag{3}$$

where Q is the spatial distribution and $\omega_0 = 2\pi f_0$ is the angular frequency associated to the source frequency f_0. The schematic of the problem is depicted in Fig. 1. Using the properties of the Dirac delta function, the acoustic potential in Eq. (2) is written as

$$\phi(\mathbf{x}, t) = \frac{1}{4\pi}\int_V Q(\mathbf{y})\exp(-i\omega_0 t_e(\mathbf{y}))\frac{\mathrm{d}\mathbf{y}}{r} \tag{4}$$

with the emission time $t_e(\mathbf{y}) = t - r(\mathbf{y})/c_0$. The preceding formula shows that the acoustic field at time t is the sum of acoustic waves emitted from all source elements at time $t_e(\mathbf{y})$ with corresponding strength $Q(\mathbf{y})$. A closed analytical form is obtained by assuming that differences in emission times are small compared with propagation time x/c_0, or equivalently that the source-receiver distance is large compared with a characteristic length scale of the source denoted by B, i.e., $x \gg B$. Expanding r around x,

$$r = x - \frac{\mathbf{x}\cdot\mathbf{y}}{x} + o(y) \tag{5}$$

at the first order in y in the phase of the integrand in Eq. (4) and at the zeroth order in y in its amplitude yields

$$\phi(\mathbf{x}, t) = \exp(-i\omega_0 t)\frac{\exp(ikx)}{4\pi}\int_V Q(\mathbf{y})\exp\left(-ik\frac{\mathbf{x}\cdot\mathbf{y}}{x}\right)\frac{\mathrm{d}\mathbf{y}}{x} \tag{6}$$

The approximations used previously are referred to as the Fraunhofer approximations [13] in the literature. The acoustic potential is then given in the geometrical far field by [9,10]

$$\phi(\mathbf{x}, t) = \exp(-i\omega_0 t)\frac{\exp(ikx)}{4\pi x}\hat{Q}\left(k\frac{\mathbf{x}}{x}\right) \tag{7}$$

where $\hat{Q}$ is the spatial Fourier transform of Q, defined by

$$\hat{Q}(\mathbf{u}) = \int_V Q(\mathbf{y})\exp(-i\mathbf{u}\cdot\mathbf{y})\,\mathrm{d}\mathbf{y} \tag{8}$$

In the free field and in the geometrical far field, the analytical solution is the product of two terms: one is the analytical solution for a point source, and the other is the Fourier transform of the spatial distribution evaluated at the wave number of modulus $k = \omega_0/c_0$ pointing in the propagation direction.[§]

For a spherical source, as $Q(\mathbf{r}) = Q(r)$, the Fourier transform depends only on the modulus of the Fourier variable, which leads to $\hat{Q}(\mathbf{u}) = \hat{Q}(u)$. Consequently, the acoustic potential is

$$\phi(\mathbf{x}, t) = \exp(-i\omega_0 t)\frac{\exp(ikx)}{4\pi x}\hat{Q}(k) \tag{9}$$

In addition, $\hat{Q}(k)$ is a real-valued function of wave number k, which implies that the phase of the solution is not modified by the source

[§]In Crighton [9] and in Dowling and Ffowcs Williams [10], the sign of the wave number $k\mathbf{x}/x$ is reversed because of the convention for the spatial Fourier transform.

distribution. Michalke [14] has studied the case of a noncompact monopole with constant source strength within a sphere. It can be shown that, outside the source sphere, the sound field is given exactly by Eq. (9). Indeed, the so-called shape factor is the Fourier transform of the spatial distribution of the source.

2. Case of a Gaussian Spatial Distribution

As an example, the case of a Gaussian spatial distribution is examined:

$$Q(\mathbf{x}) = \frac{S_0}{(\sqrt{\pi}B)^3}\exp\left(-\frac{x^2}{B^2}\right) \tag{10}$$

where S_0 is a normalization parameter set to 1 $\mathrm{m^3 \cdot s^{-1}}$. When B tends to zero, $Q(\mathbf{x})$ tends to the Dirac delta function, and the volume source tends to a point source. The spatial Fourier transform of $Q(\mathbf{x})$ is given by

$$\hat{Q}(k) = S_0 \exp\left(-\frac{k^2B^2}{4}\right) \tag{11}$$

The Gaussian spatial distribution acts as a low-pass filter, as no acoustic energy is transmitted into the geometrical far field for wavelength $\lambda = 2\pi/k \ll B$.

In this simple case, the calculation of the integral in Eq. (4) can be performed. The derivation of the analytical solution is detailed in the Appendix. The acoustic potential is written as a sum of an outgoing and an incoming spherical wave:

$$\phi(\mathbf{x},t) = \exp(-i\omega_0 t)\left[K_+\frac{\exp(ikx)}{4\pi x} - K_-\frac{\exp(-ikx)}{4\pi x}\right] \tag{12}$$

with the coefficients

$$K_\pm = S_0 \exp\left(-\frac{k^2B^2}{4}\right)\frac{1}{2}\mathrm{erfc}\left(-\frac{ikB}{2}\mp\frac{x}{B}\right) \tag{13}$$

where erfc is the complementary error function. In the geometrical far field, i.e., $x \gg B$ and K_- and K_+ tend to zero and $\hat{Q}(k)$, respectively. As expected, the analytical expression obtained in Eq. (9) is retrieved. The acoustic potential is plotted in Fig. 2 as a function of x/B for differents values of the ratio λ/B. For $x/B > 2$, the solution under the far-field approximation is in perfect agreement with the exact solution for all cases. In addition, the acoustic field is similar to that of a point source for a large value of λ/B. Note also that the acoustic potential due to a volume source has no singularity at $x/B = 0$.

B. Sources Moving at a Constant Speed

This section is concerned with the radiation of harmonic sources moving at constant speed $\boldsymbol{V}_0$. The Mach number vector and the Mach number are, respectively, defined by $\boldsymbol{M}_0 = \boldsymbol{V}_0/c_0$ and $M_0 = |\boldsymbol{M}_0| = V_0/c_0$. At the initial time $t = 0$ s, the center of the source is located at the origin of the coordinates system. The schematic of the problem is represented in Fig. 3.

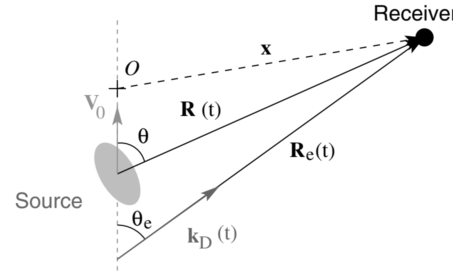

Fig. 3 Volume source moving at a constant speed V_0 in the free field.

A harmonic source is considered, and the source term is

$$S(\mathbf{x},t) = Q(\mathbf{x} - \boldsymbol{V}_0 t)\exp(-i\omega_0 t) \tag{14}$$

From Eq. (2), the solution is given by

$$\phi(\mathbf{x},t) = \frac{1}{4\pi}\int_{-\infty}^{+\infty}\int_V Q(\mathbf{y} - \boldsymbol{V}_0 t') \times \exp(-i\omega_0 t')\delta\left(t' - t + \frac{r}{c_0}\right)\frac{\mathrm{d}\mathbf{y}\,\mathrm{d}t'}{r} \tag{15}$$

Introducing $\mathbf{z} = \mathbf{y} - \boldsymbol{V}_0 t'$ leads to

$$\phi(\mathbf{x},t) = \frac{1}{4\pi}\int_{-\infty}^{+\infty}\int_V Q(\mathbf{z}) \times \exp(-i\omega_0 t')\delta\left(t' - t + \frac{R(\mathbf{z},t')}{c_0}\right)\frac{\mathrm{d}\mathbf{z}\,\mathrm{d}t'}{R(\mathbf{z},t')} \tag{16}$$

where $R(\mathbf{z},t') = |\mathbf{x} - \mathbf{z} - \boldsymbol{V}_0 t'|$ is the distance between a source element and the receiver. The analytical solution is then written as a convolution:

$$\phi(\mathbf{x},t) = \int_V Q(\mathbf{z})\phi_0(\mathbf{x} - \mathbf{z}, t)\mathrm{d}\mathbf{z} \tag{17}$$

where $\phi_0(\mathbf{x},t)$ is the solution of the problem for a point source located at the center of the volume source distribution:

$$\phi_0(\mathbf{x},t) = \frac{1}{4\pi}\int_{-\infty}^{+\infty}\exp(-i\omega_0 t')\delta\left(t' - t + \frac{R(t')}{c_0}\right)\frac{1}{R(t')}\mathrm{d}t' \tag{18}$$

In the preceding equation, $R(t') = R(\boldsymbol{0},t') = |\mathbf{x} - \boldsymbol{V}_0 t'|$ is the distance between the point source and the receiver. For the subsonic case ($M_0 < 1$), the acoustic potential is given by (see, e.g., [15])

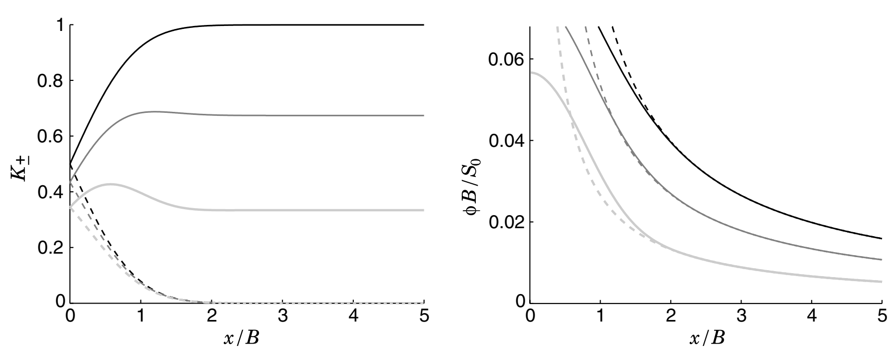

Fig. 2 a) Coefficients of the outgoing wave K_+ (solid lines) and the incoming wave K_- (dashed lines) and b) acoustic potential for the exact solution (solid lines) and for the solution under the far-field approximation (dashed lines) as a function of x/B for different values of λ/B: $\lambda/B = 100$ (black), $\lambda/B = 5$ (dark gray), and $\lambda/B = 3$ (light gray).

$$\phi_0(\mathbf{x}, t) = \frac{\exp(-i\omega_0 t_e)}{4\pi R_e(1 - M_0 \cos \theta_e)} \tag{19}$$

where t_e is the retarded time, which corresponds to the emission time of a wavepacket received at the receiver at the time t. Distance R_e is the source-receiver distance at the emission time such as $\boldsymbol{R}_e = \mathbf{x} - \boldsymbol{V}_0 t_e$ and $R_e = c_0(t - t_e)$. Finally, angles θ and θ_e are the angles between vectors $\boldsymbol{V}_0$ and $\boldsymbol{R}$ and $\boldsymbol{R}_e$, respectively.

The retarded time variables are related to those in the current time system by the relations [16]

$$\begin{cases} R_e = \frac{R}{\beta^2}\left(M_0 \cos \theta + \sqrt{M_0^2 \cos^2 \theta + \beta^2}\right), \\ \cos \theta_e = M_0 + \frac{R}{R_e} \cos \theta \end{cases} \tag{20}$$

with $\beta^2 = 1 - M^2$.

As done in the previous section, a geometrical far-field approximation is performed. Therefore, it is assumed that the distance between the source center and the receiver at the emission time is large compared with the characteristic length scale of the source, i.e., $R_e = |\mathbf{x} - \boldsymbol{V}_0 t_e| \gg B$. The phase of the acoustic potential is expanded to the first order in $\mathbf{z}$, and its amplitude is assumed to be that at the source center. To do so, the following formulas are used:

$$\begin{cases} \frac{\mathrm{d}}{\mathrm{d}\mathbf{z}} R(\mathbf{z})|_{\mathbf{z}=0} = -\frac{\boldsymbol{R}}{R}, \\ \frac{\mathrm{d}}{\mathrm{d}\mathbf{z}} M_0 \cos \theta(\mathbf{z})|_{\mathbf{z}=0} = \frac{1}{R}\left(M_0 \cos \theta \frac{\boldsymbol{R}}{R} - \boldsymbol{M}_0\right), \\ \frac{\mathrm{d}}{\mathrm{d}\mathbf{z}} \sqrt{M_0^2 \cos^2 \theta(\mathbf{z}) + \beta^2}\Big|_{\mathbf{z}=0} = \frac{1}{R} \frac{M_0 \cos \theta}{\sqrt{M_0^2 \cos^2 \theta + \beta^2}}\left(M_0 \cos \theta \frac{\boldsymbol{R}}{R} - \boldsymbol{M}_0\right) \end{cases} \tag{21}$$

Retaining only terms of the first order in z yields

$$\exp(-i\omega_0 t_e(\mathbf{z})) = \exp(-i\omega_0 t) \exp(ikR_e) \exp(-i\mathbf{k}_{\boldsymbol{D}} \cdot \mathbf{z}) \tag{22}$$

where wave number $\mathbf{k}_D$ is given by

$$\mathbf{k}_D = \frac{k}{\sqrt{M_0^2 \cos^2 \theta + \beta^2}}\left[\frac{\boldsymbol{R}}{R} + \frac{R_e}{R}\boldsymbol{M}_0\right] \tag{23}$$

Using Eq. (20), the wave number is expressed in terms of the retarded time coordinates by

$$\mathbf{k}_D = \frac{k}{1 - M_0 \cos \theta_e} \frac{\boldsymbol{R}_e}{R_e} \tag{24}$$

Wave number $\mathbf{k}_D$ points from the source at the emission time to the receiver. Its modulus is the ratio of the modulus of the wave number k to the Doppler factor $(1 - M_0 \cos \theta_e)$ and, consequently, depends on the time.

The convolution in Eq. (17) can now be written as

$$\phi(\mathbf{x}, t) = \phi_{\boldsymbol{0}}(\mathbf{x}, t) \int_V Q(\mathbf{z}) \exp(-i\mathbf{k}_D \mathbf{z})\, \mathrm{d}\mathbf{z} \tag{25}$$

Finally, the acoustic potential in the geometrical far field is given by

$$\phi(\mathbf{x}, t) = \exp(-i\omega_0 t) \frac{\exp(ikR_e)}{4\pi R_e(1 - M_0 \cos \theta_e)} \hat{Q}(\mathbf{k}_D) \tag{26}$$

which shows that for a harmonic source moving at a constant speed the spatial distribution of the source induces an additional amplification factor due to its spatial Fourier transform.

In the case of a spherical source, the acoustic potential is given by

$$\phi(\mathbf{x}, t) = \exp(-i\omega_0 t) \frac{\exp(ikR_e)}{4\pi R_e(1 - M_0 \cos \theta_e)} \hat{Q}\left(\frac{k}{1 - M_0 \cos \theta_e}\right) \tag{27}$$

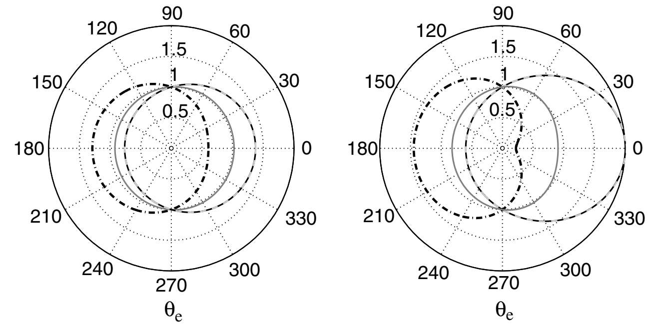

a) $M_0 = 0.15$ b) $M_0 = 0.30$

Fig. 4 Directivity diagrams for a volume source with a Gaussian spatial distribution moving at Mach numbers a) $M_0 = 0.15$ and b) $M_0 = 0.30$ for different values of λ/B: $\lambda/B = 100$ (light gray solid), $\lambda/B = 5$ (dark gray solid), $\lambda/B = 3$ (black dash–dotted), and for a point source (black dashed).

where R_e and $\cos \theta_e$ are implicit functions of the time. Keeping only the leading term in $1/R_e$ the acoustic pressure $p = -\rho_0 \partial\phi/\partial t$ is then expressed in the geometrical far field as

$$p(\mathbf{x}, t) = \rho_0 i\omega_0 \exp(-i\omega_0 t) \frac{\exp(ikR_e)}{4\pi R_e(1 - M_0 \cos \theta_e)^2} \times \hat{Q}\left(\frac{k}{1 - M_0 \cos \theta_e}\right) \tag{28}$$

For a spherical source, $\hat{Q}(k)$ is a real-valued function of wave number k. Thus, as it can be seen in Eq. (28), the acoustic pressure phase obtained for a spherical volume source is the same as that obtained for a point source in the geometrical far field. However, the amplitude and, hence, the directivity are modified. Indeed, the directivity pattern is directly related to the Fourier transform of the spatial distribution of the source. To illustrate this point, let us consider again a source with a Gaussian spatial distribution. The directivity is calculated with the expression

$$D(\theta_e) = \left(\frac{4\pi}{\omega_0 \rho_0}\right)^2 \frac{|p(\theta_e)|^2 R_e^2}{\hat{Q}^2(k)} \tag{29}$$

where the pressure $p(\theta_e)$ is given in Eq. (28). In Fig. 4, the directivity is plotted for different values of the ratio λ/B and for Mach numbers equal to 0.15 and 0.3. When $\lambda \gg B/(1 - M_0)$, the differences in emission times for all elementary sources are small compared with the time variation of the source. In that case, the source is called "compact" [16], and it behaves like a point source. Therefore, the directivity pattern obtained for the case $\lambda/B = 100$ is similar to that of a point source, as shown in Fig. 4a. For small values of λ/B, differences in emission times are significant, and discrepancies from the compact source become visible. Thus, for $\lambda/B = 5$, the amplification in the forward direction is reduced. For λ close to B, the effects of the spatial distribution are dramatically important. Thus, for $\lambda/B = 3$, the directivity pattern is reversed in comparison to that of a point source, and amplification occurs in the backward direction. This behavior is amplified when the Mach number increases, as it can be seen in Fig. 4b.

C. Comparison with Results of a Numerical Simulation in a 3-D Geometry

1. Numerical Specification

Results obtained with the analytical solution are now compared with those obtained with a numerical solver of the linearized Euler equations. High-order finite difference time-domain techniques, developed initially in the computational aeroacoustics community, are employed. Optimized finite difference schemes and selective filters over 11 points are used to compute the spatial derivative and to remove grid-to-grid oscillations, respectively, and allow accurate computation of acoustic wavelengths down to five or six times the

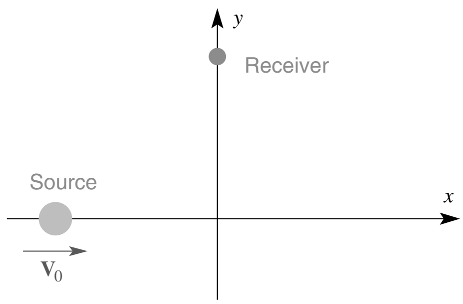

Fig. 5 Source moving along the x axis at a constant speed V_0 in a 3-D geometry.

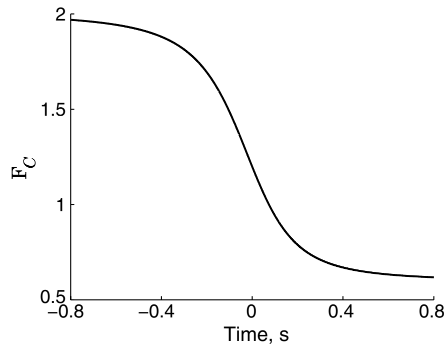

Fig. 6 Convective amplification factor as a function of the time.

spatial mesh size. For the interior points, the centered fourth-order finite difference scheme of Bogey and Bailly [17] and the sixth-order selective filter of Bogey et al. [18] are chosen. For the boundary points, the noncentered finite difference schemes and the noncentered selective filters of Berland et al. [19] are used. The filtering coefficient is set to 0.2 for all filters except at the end points, at which the filtering coefficient is 0.01. The time integration is performed with the six-step fourth-order Runge–Kutta algorithm of Berland et al. [20]. At the outer boundaries, perfectly matched layers [21] are employed in the splitting form, as done by Hornikx et al. [22]. Simulations presented in this section are performed in a 3-D geometry. The size of the numerical domain is $[-100\ \mathrm{m}; 100\ \mathrm{m}] \times [-5\ \mathrm{m}; 30\ \mathrm{m}] \times [-5\ \mathrm{m}; 5\ \mathrm{m}]$. The mesh is uniform, and the mesh size is $\Delta x = \Delta y = \Delta z = 0.1$ m. The CFL number defined by $\mathrm{CFL} = c_0 \Delta t / \Delta x$ is set to one. Around 6000 time iterations are performed. The source is implemented through the mass source term. At time $t = 0$ s, the center of the source is located at $x = 0$ m, $y = 0$ m, and $z = 0$ m.

As depicted in Fig. 5, the source is moving in the free field along the x axis at speed $V_0 = 100\ \mathrm{m \cdot s^{-1}}$. The Mach number is equal to 0.3. The receiver is located at $x_R = 0$ m, $y_R = 25$ m, and $z_R = 0$ m. As indicated in Sec. II.B, there are two amplification factors compared with the case of a nonmoving source. The first one is related to the spatial distribution of the source and is defined by

$$F_S(t) = \left| \frac{\hat{Q}(\mathbf{k}_D)}{\hat{Q}(\mathbf{k})} \right| \tag{30}$$

The second one, called the convective amplification factor,

$$F_C(t) = \frac{1}{(1 - M_0 \cos \theta_e)^2} \tag{31}$$

is due to the source motion and is related to the Doppler factor. It is plotted as a function of the time in Fig. 6. Typically, it is larger than one as the source approaches the receiver and smaller than one as the source recedes from the receiver.

2. *Spherical Source*

This section is concerned with a spherical source. The spatial distribution of the source is Gaussian [see Eq. (10)] with $B = 0.36$ m. Two frequencies $f_0 = 50$ and 300 Hz are considered. The spatial Fourier transform of the source distribution is represented as a function of the frequency in Fig. 7a. The variations of $\hat{Q}(k_D)$ during the source motion are also shown for both frequencies in bold lines. The corresponding source amplification factor given in Eq. (30) is plotted as a function of the time in Fig. 7b. For $f_0 = 50$ Hz, the maximum of $k_D B$ is 0.47. Consequently, the source can be considered as compact. In this case, the term $\hat{Q}(k_D)/S_0$ remains close to one, and the amplification factor due to the source is also close to one, as seen in Fig. 7b. Thus, the spatial distribution does not play an important role and the source is expected to behave like a point source. The source frequency is now increased to $f_0 = 300$ Hz. The maximum of $k_D B$ is 2.8, and the source is not compact anymore. In this case, the Fourier transform $\hat{Q}(k_D)$ varies over a wide range, and the source amplification factor has large values. Note that, for the Gaussian distribution, unlike the convective amplification factor, F_S is lower than unity as the source approaches the receiver and is greater than unity as the source recedes from the receiver.

A total amplification factor $F = F_S F_C$ is calculated and is shown as a function of the time in Fig. 8 for both frequencies. For

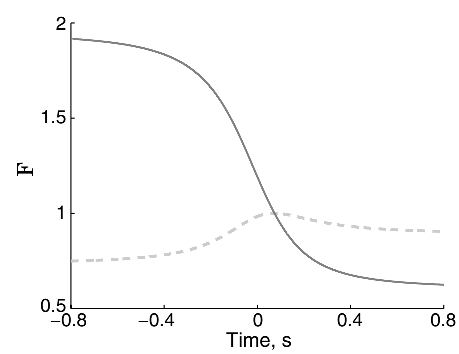

Fig. 8 Total amplification factor as a function of the time for $f_0 =$ 50 Hz (dark gray solid) and $f_0 = 300$ Hz (light gray dashed).

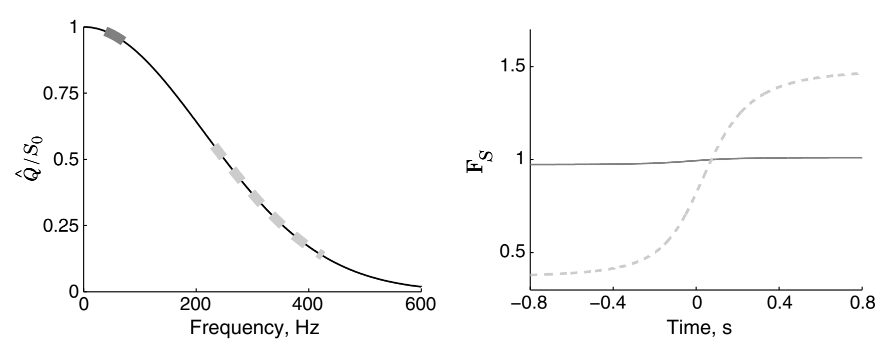

Fig. 7 a) spatial Fourier transform $\hat{Q}/S_0$ (thin line) as a function of the frequency and values taken by $\hat{Q}(k_D)/S_0$ during the source motion (thick lines) and b) amplification factor due to the source as a function of the time for $f_0 = 50$ Hz (dark gray solid) and $f_0 = 300$ Hz (light gray dashed).

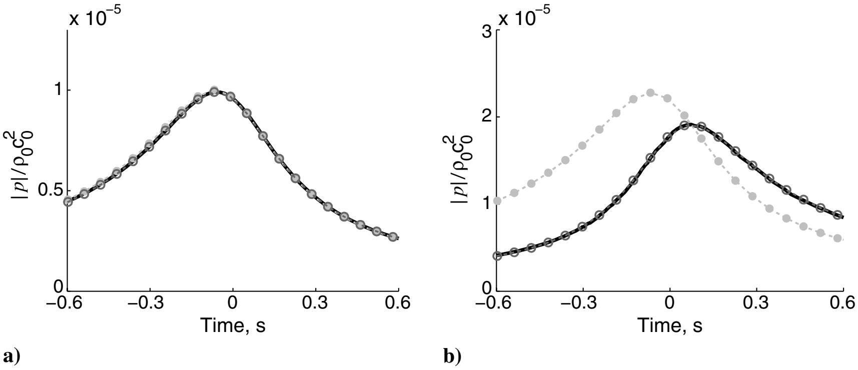

Fig. 9 Pressure amplitude $|p|$ at the receiver as a function of the time a) for $f_0 = 50$ Hz and b) for $f_0 = 300$ Hz: numerical solution (black solid line) and analytical solutions for a point-source (light gray dashed line with closed circles) and for a volume source using the geometrical far-field approximation (dark gray dashed line with open circles). A spherical source is considered.

$f_0 = 50$ Hz, the total amplification factor is close to the convective amplification factor, as the source amplification factor is close to one. For $f_0 = 300$ Hz, because the time variations of the source amplification factor are larger than those of the convective amplification factor, F has larger values when the source recedes from the receiver, unlike the case of a point source.

The amplitudes of the acoustic pressure obtained with the numerical simulation and calculated with the analytical solution for a volume source under the geometrical far-field approximation given in Eq. (28) and for a point source with the directivity obtained in nonmoving conditions,

$$p_0(\mathbf{x}, t) = \rho_0 i\omega_0 \exp(-i\omega_0 t)\frac{\exp(ikR_e)}{4\pi R_e(1 - M_0 \cos\theta_e)^2}\hat{Q}(\mathbf{k}) \quad (32)$$

are represented in Fig. 9 as a function of the time. Figure 9a shows that for $f_0 = 50$ Hz the point-source solution is in a good agreement with the numerical solution. The solution for a volume source under the geometrical far-field approximation gives similar results. For $f_0 = 300$ Hz, it can be observed in Fig. 9b that the pressure amplitude determined with the analytical solution for a point source is not consistent with that of the numerical solution. On the contrary, the analytical solution obtained for a volume source in the geometrical far field allows one to retrieve the time variations of the pressure amplitude.

As noticed in Sec. II.B, the volume source distribution for a spherical source induces only an amplitude modulation of the acoustic pressure compared with a point source, because $\hat{Q}(\mathbf{k})$ is a real-valued function of k. The phase of the acoustic pressure is the same, and the Doppler shift must be obtained in particular. To highlight this point, a time-frequency analysis is performed. The time-domain pressure signal, whose amplitude is plotted in Fig. 9 as a function of the time, is divided into segments of 0.075 s, on each of which a Fourier transform is performed. Figure 10 shows the

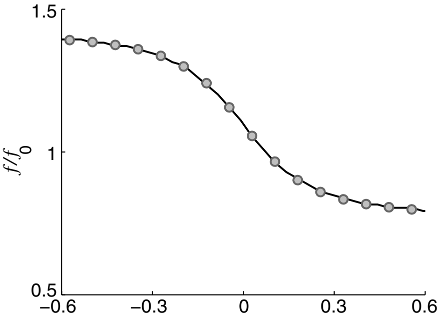

Fig. 10 Instantaneous frequency of the pressure signal as a function of the time for $f_0 = 50$ Hz: numerical solution (black solid line) and analytical solutions for a point-source (light gray dashed line with closed circles) and for a volume source using the geometrical far-field approximation (dark gray dashed line with open circles).

instantaneous frequency of the pressure signal as a function of the time for $f_0 = 50$ Hz. The Doppler frequency $f_D = f_0/(1 - M_0 \cos\theta_e)$ (see, e.g., [15]) is also represented. As expected, the Doppler frequency shift is retrieved in the simulations. The case $f_0 = 300$ Hz has not been shown, because the results are exactly the same.

To reproduce a point source, the characteristic length scale of the volume source must be chosen to be as small as possible. The spatial discretization of the source region must be, however, sufficiently fine to capture the variations of the source distribution. One can then wonder about the minimal number of grid points required to discretize the source region in order to obtain an accurate solution. A test case is now considered to evaluate the variations of the error as a function of the ratio of the characteristic length of the source to the mesh size. The frequency of the source is set to $f_0 = 340$ Hz, and the corresponding wavelength is $\lambda = 1$ m. The numerical domain is $[-50\text{ m}; 50\text{ m}] \times [-5\text{ m}; 10\text{ m}] \times [-5\text{ m}; 5\text{ m}]$. The mesh is uniform, and several simulations are performed with a mesh size ranging from $\Delta x = 0.05$ to 0.125 m, corresponding to waves discretized between 20 and 8 points per wavelength. The CFL number is reduced to 0.7 to ensure negligible time-integration errors. The source is moving along the x axis at the constant speed $V_0 = 100\ \mathrm{m \cdot s^{-1}}$. A receiver is located at (0 m, 5 m, 0 m).

The error at the receiver is evaluated using the criterion

$$L_2\left(\frac{B}{\lambda}, \frac{\Delta x}{\lambda}\right) = \sqrt{\frac{1}{2t_p}\int_{-t_p}^{t_p}\left|\frac{|p| - |p_{\mathrm{ana}}|}{|p_{\mathrm{ana}}|}\right|^2} \quad (33)$$

with $t_p = 0.3$ s and where p_{ana} is the analytical solution given in Eq. (17). The error is represented in Fig. 11 as a function of $B/\Delta x$ for four values of the number of points per wavelength $\lambda/\Delta x$, which are $\lambda/\Delta x = 8$, 10, 15, and 20. All the curves have a similar behavior. The error is large for $B\Delta x < 0.5$ and decreases as $B/\Delta x$ increases up to $B/\Delta x = 1$, approximately. For $B/\Delta x > 1$, the error is nearly

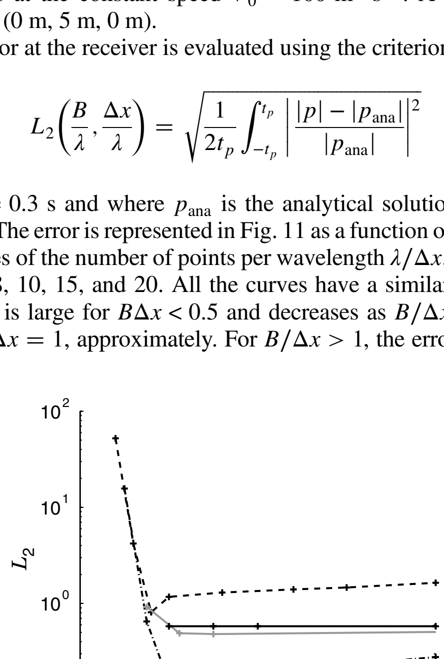

Fig. 11 Error L_2 as a function of $B/\Delta x$ for four values of the number of points per wavelength: $\lambda/\Delta x = 8$ (black dashed), $\lambda/\Delta x = 10$ (black dash-dotted), $\lambda/\Delta x = 15$ (gray solid), and $\lambda/\Delta x = 20$ (black solid).

constant and depends only on the number of points per wavelength $\lambda/\Delta x$. This shows that as long as $B \geq \Delta x$ the spatial discretization of the source does not play a role in the accuracy of the results.

3. *Finite-Length Line Source*

Finite-length line sources are commonly used in transportation noise applications, for instance to model the entire train [23]. It is then interesting to demonstrate that they can be taken into account in time-domain simulations using a linearized Euler equations solver. A finite-length line source directed along the x axis is introduced using the source term:

$$Q(x, y, z) = \frac{S_0}{\pi B^2} \exp\left(-\frac{y^2 + z^2}{B^2}\right) q(x) \tag{34}$$

with the function

$$q(x) = \begin{cases} \frac{1}{2A}, & \text{if } |x| \leq A \\ \frac{1}{2A} \exp\left(-\frac{(|x|-A)^2}{B^2}\right), & \text{if } |x| \geq A \end{cases} \tag{35}$$

To avoid any singularity, the volume source distribution in the transverse directions y and z is Gaussian. For the same reason, the decrease of the volume distribution along the x direction is ensured to be continuous using a Gaussian function. The parameters of the finite-length line source are set to $A = 0.5$ m and $B = 0.12$ m.

The Fourier transform of the source term is written

$$\hat{Q}(k_x, \mathbf{k}_t) = S_0 \exp\left(-\frac{k_t^2 B^2}{4}\right) \hat{q}(k_x) \tag{36}$$

where $\mathbf{k}_t = (k_y, k_z)$ is the transverse wave number. The quantity $\hat{q}(k_x)$ is given by

$$\hat{q}(k_x) = \left[\frac{\sin(k_x A)}{k_x A} + \frac{\sqrt{\pi} B}{2A} \exp\left(-\frac{k_x^2 B^2}{4}\right) \times \left(\cos(k_x A) - \sin(k_x A) f\left(\frac{k_x B}{2}\right)\right)\right] \tag{37}$$

with $f(x) = (\mathrm{erfi}(x) - \mathrm{erfi}(-x))/2$, where erfi is the imaginary error function. When B tends to zero, $Q(x)$ tends to the classical finite-length line source and

$$\hat{Q}(k_x, \mathbf{k}_t) \underset{B\to 0}{=} S_0 \frac{\sin(k_x A)}{k_x A} \tag{38}$$

which is the expected result for the directivity of such a finite-length line source [24].

As for the spherical source in the previous section, the frequencies $f_0 = 50$ and 300 Hz are considered. The pressure amplitudes obtained in both cases from the numerical solution and from the analytical solutions for a point source with the directivity obtained in the nonmoving configuration given in Eq. (32) and for the volume source in the geometrical far field given in Eq. (28) are represented in Fig. 12 as a function of the time. For the first frequency $f_0 = 50$ Hz, the source can be considered as compact because the maximum of $k_D A$ is 0.65. As a consequence, the source behaves like a point source, and its directivity is not modified by its motion. This is clearly seen in Fig. 12a, where the pressure amplitude obtained in the numerical simulation is very close to that obtained in Fig. 9a for the spherical source. In addition, the analytical solution for a volume source in geometrical far field is in a very good agreement with the numerical solution. Some discrepancies are seen between the numerical solution and the analytical solution for a point source for $t < 0$. For the frequency $f_0 = 340$ Hz, as the maximum of $k_D A$ is 3.9, the source is not compact. As shown in Fig. 12b, there is a clear effect of the directivity of the finite-length line source on the acoustic pressure. In particular, due to the term $\sin(k_x A)/(k_x A)$, the acoustic pressure is zero at $t = -0.2$, -0.05, and 0.3 s. The pressure amplitude obtained with the numerical solution is in a very good agreement with that obtained with the analytical solution for a volume source in the geometrical far field, which shows that the modeling of such a source in time-domain solvers is possible. Moreover, the source motion plays an important role on the directivity of the source, as the differences between the analytical solutions for a point source and for a volume source in the geometrical far field are large.

III. Broadband Moving Source Above a Ground Surface in a 3-D Geometry

This section deals with numerical simulations of a broadband source moving above a flat impedance ground. Few studies have been published investigating moving sources above a ground surface of finite impedance. Among them, Norum and Liu [25] have developed an analytical solution for a harmonic point source moving at a constant speed and at a constant height in the acoustic far field, based on a Lorentz transformation. A correction for the reflected wave has been done by Li et al. [26]. For other configurations, analytical solutions based on a heuristic approach [27] have been proposed. As noticed by Ochmann [12], all these studies assume that the surface impedance is frequency independent, which is a crude approximation for natural grounds. Recently, an analytical solution has also been proposed [12] for an impedance plane whose surface impedance varies linearly with the frequency. Numerical solutions using time-domain solvers can account for any frequency variations of the impedance and are then well suited for the study of sound radiation from moving sources above an impedance ground. In this section, SPLs obtained for a rigid ground and for a ground surface of finite impedance are compared. A schematic of the problem is depicted in Fig. 13.

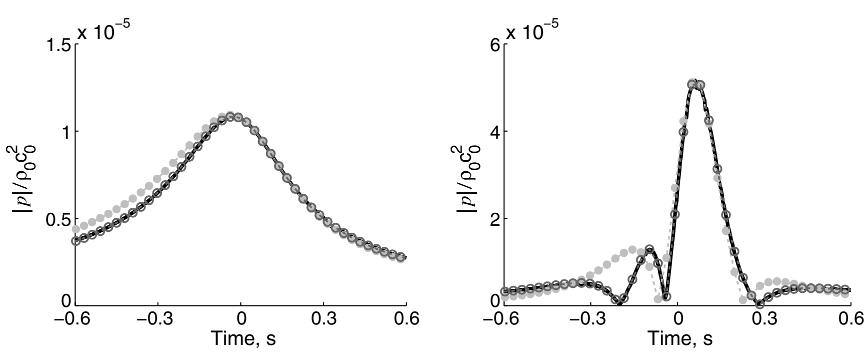

a) b)

Fig. 12 Pressure amplitude $|p|$ at the receiver as a function of the time a) for $f_0 = 50$ Hz and b) for $f_0 = 300$ Hz: numerical solution (black solid line) and analytical solutions for a point-source (light gray dashed line with closed circles) and for a volume source using the geometrical far-field approximation (dark gray dashed line with open circles). A finite-length line source is considered.

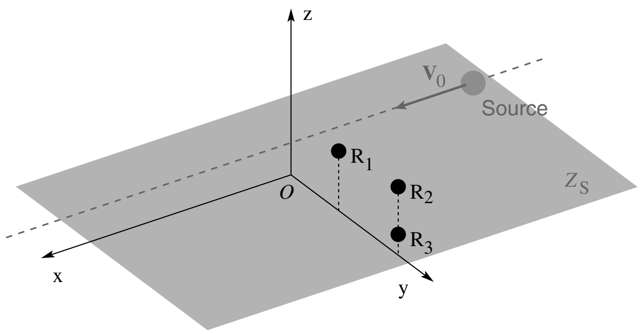

Fig. 13 Source moving above a flat surface of impedance Z_S along the x axis at a constant speed V_0 in a 3-D geometry. Three receivers R_1, R_2, and R_3 are considered.

A. Numerical Specification

A Cartesian grid of $2001 \times 351 \times 72$ points is used for the simulations. The mesh grid is uniform and $\Delta x = \Delta y = \Delta z = 0.1$ m. The domain size is then $[-100 \text{ m}; 100 \text{ m}] \times [-5 \text{ m}; 30 \text{ m}] \times [0 \text{ m}; 7.1 \text{ m}]$. The CFL number is set to unity, and 12,000 time iterations are performed. At the ground surface, the time-domain impedance boundary conditions proposed by Cotté et al. [2] are implemented. They are based on a recursive convolution technique, introduced in acoustics by Reymen et al. [28] for sound propagation in a duct.

The source is moving along the x axis at a constant height $z = 2.1$ m and at a constant speed $V_0 = 50 \text{ m} \cdot \text{s}^{-1}$. The Mach number is then equal to $M_0 = 0.15$. At the initial simulation time, the source is located at $x = -95$ m. The source term

$$S(\mathbf{x}, t) = Q(\mathbf{x} - \mathbf{V}_0 t) s(t) \tag{39}$$

is implemented in the numerical solver. The source signal $s(t)$ is a random signal constructed so that its one-sided power spectral density (PSD) is a Gaussian function:

$$S_{ss} = s_0 \exp\left[-2\frac{(f - f_c)^2}{f_b^2}\right] \tag{40}$$

where s_0 is a normalization parameter set to 1×10^{-4}. The central frequency f_c is chosen as 300 Hz. The parameter f_b controls the decrease of the Gaussian and is set to 100 Hz. The time-domain signal $s(t)$ is obtained by multiplying the Fourier transform of a synthetized white noise signal by the desired spectrum [see Eq. (40)] in the frequency domain and by doing an inverse Fourier transform of the result. The PSD of the signal is plotted as a function of the frequency in Fig. 14. It is observed that the frequency content of the source is significant for frequencies between 200 and 400 Hz. As $s(t)$ is random, the mean value of the PSD of the pressure is evaluated by averaging the PSD of the pressure over the number of realizations of the source signal. A tradeoff has then to be found between a satisfactory convergence of the results and the computational cost, which is important for 3-D simulations. Ten realizations of the random source signal are performed here for each surface impedance case, and the time-frequency decompositions presented in the next sections are obtained by averaging the results.

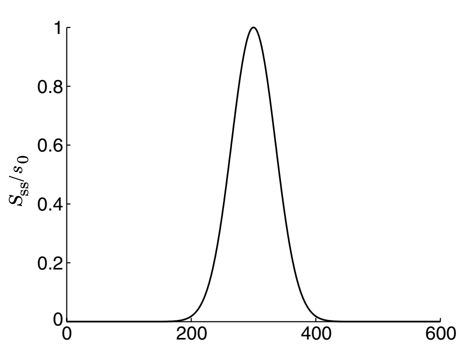

Fig. 14 PSD of the source signal as a function of the frequency.

The spatial distribution of the source Q is Gaussian, with $B = 0.12$ m [see Eq. (10)]. As discussed in Sec. II.C.2, the coarse discretization of the source distribution is not expected to reduce the accuracy of the results. As the parameter $k_D B = k_0 B/(1 - M_0 \cos\theta_e)$ has a maximum of one reached for the maximum frequency of interest $f = 400$ Hz, the source can be considered as compact and is expected to behave like a point source.

B. Rigid Ground Surface

1. Numerical Results

First, a rigid ground surface is investigated. Two receivers denoted as R_1 and R_2 and located, respectively, at $x = 0$ m, $y = 4.9$ m, and $z = 3$ m and at $x = 0$ m, $y = 24.9$ m, and $z = 3.5$ m are considered. The instantaneous PSDs obtained at these receivers are plotted as a function of the time and the frequency in Fig. 15. The reference pressure is set to $p_{\text{ref}} = 2 \times 10^{-5}$ Pa. The Doppler shift is clear, as the acoustic pressure has a higher frequency content when the source approaches the receiver than when the source recedes from the receiver. As for a nonmoving source, the ground effects are important. As an illustration, strong destructive and constructive interferences are clearly visible.

Reflection from the rigid ground can be interpreted as an additional contribution from an image source located symmetrically to the source with respect to the ground plane. Therefore, from Eq. (28), the acoustic pressure for a harmonic point source moving at a constant speed above a rigid ground is given by

$$p_0(\mathbf{x}, t) = \rho_0 i\omega_0 \exp(-i\omega_0 t)\left[\frac{\exp(ikR_{e,1})}{4\pi R_{e,1}(1 - M_0 \cos\theta_{e,1})^2} + \frac{\exp(ikR_{e,2})}{4\pi R_{e,2}(1 - M_0 \cos\theta_{e,2})^2}\right] \tag{41}$$

In the preceding equation, $(R_{e,1}, \cos\theta_{e,1})$ and $(R_{e,2}, \cos\theta_{e,2})$ are the retarded time coordinates whose origin is, respectively, the source and the image source. Minima of the acoustic pressure modulus occur when $k(R_{e,2} - R_{e,1}) = (1 + 2n)\pi$ or equivalently when $R_{e,2} - R_{e,1} = (1/2 + n)\lambda$ for n positive integer. The destructive interference is directly linked to the wave number $k = \omega_0/c_0$. However, from the observer's point of view, it appears at a different frequency due to the Doppler shift. Because the source is close to the ground, one has $\cos\theta_{e,2} \approx \cos\theta_{e,1}$, and the frequency at the observer is assumed to be $f_D = f_0/(1 - M_0 \cos\theta_{e,1})$. The curve corresponding to the case $n = 0$ for the two receivers is plotted in a dashed line in Fig. 15. A good agreement is found for the destructive interference location. A second interference, related to $n = 1$, is distinguished in Fig. 15a. For other values of n, interference patterns cannot be clearly seen and the corresponding curves are not plotted.

2. Comparison with an Analytical Solution

The numerical solution is now compared with an analytical solution. From Eq. (41), the instantaneous PSD for a broadband moving source with a spherical volume distribution above a rigid ground is given by

$$S_{pp}(\mathbf{x}, f, t) = S_{ss}(f)|\hat{Q}(k_D)|^2 \rho_0^2 \omega^2 \times \left|\frac{\exp(ikR_{e,1})}{4\pi R_{e,1}(1 - M_0 \cos\theta_{e,1})^2} + \frac{\exp(ikR_{e,2})}{4\pi R_{e,2}(1 - M_0 \cos\theta_{e,2})^2}\right|^2 \tag{42}$$

It is represented as a function of the time and the frequency at the observer f_D in Fig. 16 at the same receivers as in Fig. 15. Note that, unlike the analytical solution, the time-frequency decompositions obtained with the numerical solution are a function of the frequency at the observer, without any assumption. The numerical solution compares favorably to the analytical solution. Of course, the time-

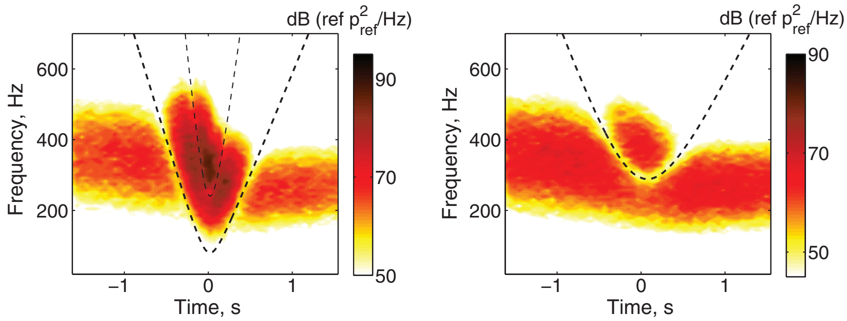

a) b)

Fig. 15 Instantaneous PSD of the acoustic pressure in decibels (ref $p_{\mathrm{ref}}^2/\mathrm{Hz}$) as a function of the time and the frequency obtained from the numerical solution at the receiver a) R_1 and b) R_2. The dashed lines represent the destructive interference location. A rigid ground is considered.

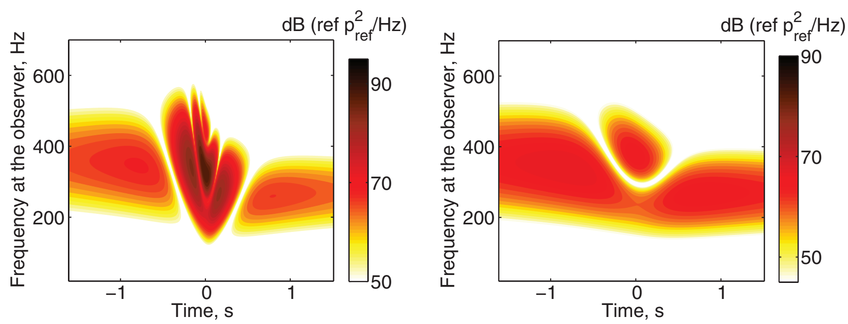

a) b)

Fig. 16 Instantaneous PSD of the acoustic pressure in decibels (ref $p_{\mathrm{ref}}^2/\mathrm{Hz}$) as a function of the time and the frequency obtained from the analytical solution at the receiver a) R_1 and b) R_2. A rigid ground is considered.

frequency decompositions in Fig. 15 appear more fuzzy than in Fig. 16 because of the initial random signals.

A more quantitative comparison is now done by considering the instantaneous SPL, which is obtained by integrating the one-sided PSDs over frequencies:

$$\mathrm{SPL}(\mathbf{x}, t) = \int_0^{+\infty} S_{pp}(\mathbf{x}, f, t)\,\mathrm{d}f \tag{43}$$

Figure 17 shows the instantaneous SPL determined from the analytical and numerical solutions as a function of the time. For the receiver R_1, due to the constructive interference pattern, there is almost 20 dB difference in the SPL when the source is in front of the receiver and when the source is far from the receiver. For the receiver R_2, the amplitude of the variations of the SPL is reduced. For both cases, a very good agreement is obtained between the SPL computed from the analytical and numerical solutions, as the maximum difference is about 0.5 dB. Because the calculation of the SPL is done by integrating the PSD of the pressure over frequencies, there is an averaging effect, and the comparisons of the SPL appear more favorably than the comparisons of the time-frequency decompositions represented in Figs. 15 and 16.

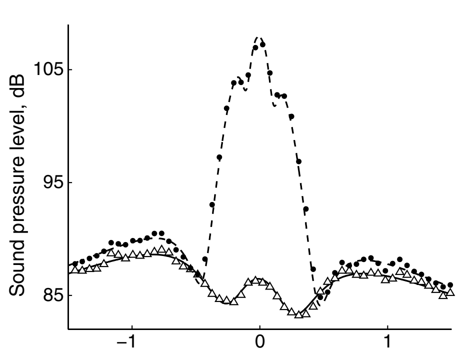

Fig. 17 Instantaneous SPL in decibels as a function of the time obtained from the analytical solution at R_1 (dashed line) and R_2 (solid line) and from the numerical solution at R_1 (•) and R_2 (Δ). A rigid ground is considered.

C. Impedance Ground Surfaces

Two types of ground surface impedances are now investigated: a grassy ground modeled by the Miki one-parameter model [29] of a semi-infinite ground layer of airflow resistivity $\sigma = 100$ kPa · s · m^{-2} and a snowy ground modeled by the Miki one-parameter model of a rigidly backed layer of thickness $d = 10$ cm and of airflow resistivity $\sigma = 10$ kPa · s · m^{-2}. The values of σ used here are typical for these kinds of natural grounds [30]. These surface impedance models have already been used in Dragna et al. [3] to study long-range sound propagation in a stratified atmosphere. Accurate modeling of natural grounds would require more elaborate models, such as the Attenborough fourth-parameter model [31], which includes also the porosity and the tortuosity of the medium. However, as remarked in [32], it is generally difficult from outdoor measurements to deduce more than two impedance model parameters. That is the main reason why one-parameter impedance models continue to be used for outdoor surfaces.

The instantaneous PSD obtained at the receiver R_1 is represented as a function of the time and the frequency for the two impedance models in Fig. 18. In comparison with the rigid boundary case (see Fig. 15a), it is dramatically modified. In particular, the pressure levels are lower when the source approaches and recedes from the receiver. Note also that the strong destructive interference pattern is suppressed. However, one can distinguish on the time-frequency decompositions an interference pattern around $t = 0$ s. The differences on the PSD computed for the two impedance models are also significant. Indeed, the PSD obtained in the case of a snowy ground is globally larger than that obtained in the case of a grassy ground. However, the global shape is similar.

Figure 19 shows the PSDs in the far field at the receiver R_3, located at $x = 0$ m, $y = 24.9$ m, and $z = 0.5$ m for the two impedance models. The receiver R_3 is chosen closer to the ground surface than

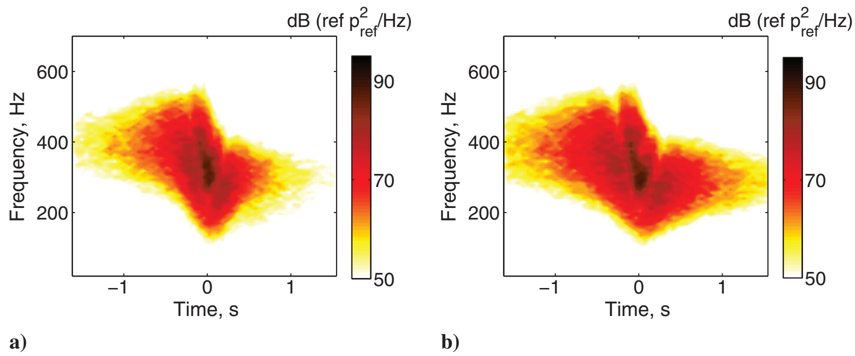

Fig. 18 Instantaneous PSD of the acoustic pressure in decibels (ref $p_{\mathrm{ref}}^2/\mathrm{Hz}$) as a function of the time and the frequency at the receiver R_1 for a) a grassy ground and b) a snowy ground.

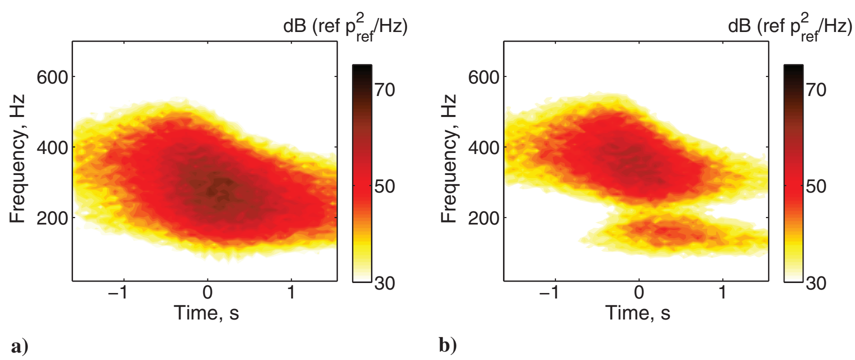

Fig. 19 Instantaneous PSD of the acoustic pressure in decibels (ref $p_{\mathrm{ref}}^2/\mathrm{Hz}$) as a function of the time and the frequency at the receiver R_3 for a) a grassy ground and b) a snowy ground.

R_2 to highlight the ground effect. For the grassy ground, the time-frequency decomposition is typical of a moving source, and the Doppler shift is clearly seen. For the snowy ground, it is more complex. Indeed, a low-frequency contribution is significant when the source recedes from the receiver, i.e., when the frequency content of the source is in the low-frequency range. This can be related to a surface wave, which has already been exhibited for this impedance model in a previous study [3].

Finally, the instantaneous SPLs obtained for the different boundary conditions are compared at the receivers R_1 and R_3 in Fig. 20. For R_1, far from the receiver, the SPL is greater for the rigid case by almost 10 dB. Close to the receiver, for $t = -0.5$ and 0.5 s, the SPL becomes larger for the finite-impedance ground surfaces because of the strong destructive interferences observed in Fig. 15. In addition, as noticed earlier, the pressure levels are smaller for the grassy ground than for the snowy ground. For R_3, the SPL obtained for the rigid ground is remarkably large compared with that obtained for the finite-impedance ground surfaces, of about 20 dB. It can also be noted that the SPL for the grassy ground is larger in the backward direction than in the forward direction unlike the rigid case. Indeed, transmission of acoustic waves into the ground is essentially a frequency-dependent phenomenon. Therefore, more or less energy can be transmitted into the ground according to the frequency content of the signal. Moreover, the values of the SPL are close for the finite-impedance cases in which the source approaches the receiver, whereas when the source recedes from the receiver the SPL for the grassy ground is 10 dB larger than that for the snowy ground.

IV. Conclusions

The modeling of moving sources in a time-domain solver has been examined using distributed volume sources. The effect of the volume source distribution on the acoustic field has been studied in the geometrical far field. For a nonmoving source, the source distribution acts as a filter, as the Fourier transform of the spatial distribution modulates the pressure. For a moving source, the behavior is more complex as the Fourier transform is evaluated at a wave number that depends on the time and on the source speed. In addition, the

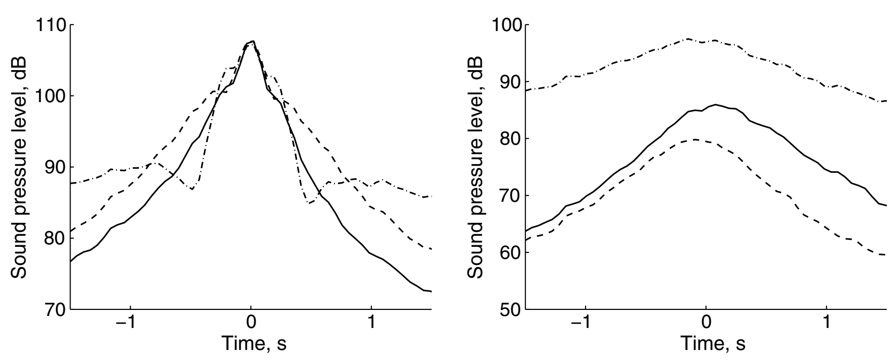

Fig. 20 Instantaneous SPL of the acoustic pressure in decibels as a function of the time at a receiver located a) at R_1 and b) at R_3 for a grassy ground (solid), for a snowy ground (dashed), and for a rigid ground (dash-dotted).

directivity of a compact source is similar to that of a point source. When the emitted wavelength is in the order of the characteristic source length, the directivity is, however, strongly modified and, in the case of a spherical source, more energy can be radiated in the backward direction than in the forward direction. This behavior has been reproduced in the results of numerical simulations performed with a solver of the linearized Euler equations. The Doppler effect has also been exhibited in the simulated waveforms. Finally, simulations of a broadband source moving at a constant speed above an impedance ground surface in a 3-D geometry have been performed for a rigid ground, a grassy ground, and a snowy ground. It has been shown that the instantaneous SPLs were dramatically different, depending on the boundary conditions. In particular, as for a nonmoving source, strong destructive interferences have been observed for a rigid ground. For ground surfaces of finite impedance, these strong interferences do not appear anymore in the considered frequency bandwidth. Moreover, complex patterns have been exhibited close to the ground. In particular, a low-frequency contribution has been observed for the snowy ground case.

The feasibility of numerical time-domain simulations of moving sources in a 3-D geometry has been demonstrated. This work has been concerned with monopole acoustic sources and finite-length line sources but can be extended to dipoles and quadrupoles, which are relevant for aerodynamic noise. Another extension of the study would be to consider incoherent sources, as only coherent sources have been here investigated. For transportation noise applications, engineering models can then be validated against results obtained with reference time-domain solvers. These solvers can also be used to consider complex scenarios, such as a train pass-by in a realistic railway site, with a topography and a mixed impedance ground. Moreover, to account for more realistic sources, coupling with other computational models can be done. For instance, large-eddy simulations of pantographlike sources can be performed to provide input data to the solver of the linearized Euler equations to compute long-range sound propagation in a complex environment. This approach will be followed in future work.

Appendix: Acoustic Potential for a Source with a Gaussian Spatial Distribution

The calculation of the acoustic potential for a harmonic source with a Gaussian spatial distribution is performed. The time dependence $\exp(-i\omega_0 t)$ and the normalization factor S_0 are omitted for clarity. First, the acoustic potential is written in this case as [see Eq. (4)]

$$\phi(\mathbf{x}) = \frac{1}{4\pi^{5/2}B^3}\int_V \frac{\exp(ik|\mathbf{x}-\mathbf{y}|)}{|\mathbf{x}-\mathbf{y}|}\exp\left(-\frac{|\mathbf{y}|^2}{B^2}\right)\mathrm{d}\mathbf{y} \tag{A1}$$

Making use of the change of variables $\mathbf{r} = \mathbf{y} - \mathbf{x}$ yields

$$\phi(\mathbf{x}) = \frac{1}{4\pi^{5/2}B^3}\int_V \frac{\exp(ik|\mathbf{r}|)}{|\mathbf{r}|}\exp\left(-\frac{|\mathbf{x}+\mathbf{r}|^2}{B^2}\right)\mathrm{d}\mathbf{r} \tag{A2}$$

To calculate the integral, spherical coordinates $\mathbf{r} = (r\cos\theta\sin\phi, r\sin\theta\sin\phi, r\cos\phi)$ are introduced. Because of the spherical symmetry of the problem, the acoustic potential depends only on the distance to the source center. Without loss of generality, we choose $\mathbf{x} = (0,0,x)$. Equation (A2) becomes

$$\phi(x) = \frac{1}{4\pi^{5/2}B^3}\int_0^\infty\int_0^{2\pi}\int_0^\pi \exp(ikr) \times \exp\left(-\frac{r^2+x^2+2xr\cos\phi}{B^2}\right) r\sin\phi\,\mathrm{d}r\,\mathrm{d}\theta\,\mathrm{d}\phi \tag{A3}$$

Integrating over θ gives

$$\phi(x) = \frac{1}{2\pi^{3/2}B^3}\exp\left(-\frac{x^2}{B^2}\right)\int_0^\infty r\exp(ikr)\exp\left(-\frac{r^2}{B^2}\right) \times \int_0^\pi \sin\phi\exp\left(-\frac{2xr\cos\phi}{B^2}\right)\mathrm{d}\phi\,\mathrm{d}r \tag{A4}$$

Then, the expression for the acoustic potential can be reduced to a single integral:

$$\phi(x) = \frac{1}{4\pi^{3/2}Bx}\exp\left(-\frac{x^2}{B^2}\right)\int_0^\infty \exp(ikr) \times\exp\left(-\frac{r^2}{B^2}\right)\left[\exp\left(-\frac{2xr\cos\phi}{B^2}\right)\right]_0^\pi \mathrm{d}r \tag{A5}$$

The acoustic field is now split into incoming and outgoing waves $\phi(x) = \phi_+(x) - \phi_-(x)$, with

$$\phi_\pm(x) = \frac{1}{4\pi^{3/2}Bx}\exp\left(-\frac{x^2}{B^2}\right)\int_0^\infty \exp\left(ikr - \frac{r^2 \mp 2xr}{B^2}\right)\mathrm{d}r \tag{A6}$$

A closed analytical form for the terms $\phi_\pm(x)$ results from the change of variables $u = r/B + x/B \pm ikB/2$:

$$\phi_\pm(x) = \frac{1}{4\pi}\frac{\exp(\pm ikx)}{2x}\exp\left(-\frac{k^2B^2}{4}\right)\mathrm{erfc}\left(-\frac{ikB}{2}\mp\frac{x}{B}\right) \tag{A7}$$

Finally, the acoustic potential is expressed under the form

$$\phi(x) = \exp\left(-\frac{k^2B^2}{4}\right)\frac{1}{2}\left[\frac{\exp(ikx)}{4\pi x}\mathrm{erfc}\left(-\frac{ikB}{2}-\frac{x}{B}\right) - \frac{\exp(-ikx)}{4\pi x}\mathrm{erfc}\left(-\frac{ikB}{2}+\frac{x}{B}\right)\right] \tag{A8}$$

which corresponds to Eq. (12).

Acknowledgments

Support by Centre National de la Recherche Scientifique and SNCF is gratefully acknowledged. This work was conducted in the framework of the LabEx CeLyA ("Centre Lyonnais d'Acoustique," Grant No. ANR-10-LABX-60). It was granted access to the high-performance computing resources of IDRIS under the allocation 2013-022203 made by Grand Equipement National de Calcul Intensif (GENCI).

References

[1] Van Renterghem, T., and Botteldooren, D., "Numerical Simulation of the Effect of Trees on Downwind Noise Barriers Performance," *Acta Acustica United with Acustica*, Vol. 89, No. 5, 2003, pp. 764–778.

[2] Cotté, B., Blanc-Benon, Ph., Bogey, C., and Poisson, F., "Time-Domain Impedance Boundary Conditions for Simulations of Outdoor Sound Propagation," *AIAA Journal*, Vol. 47, No. 10, 2009, pp. 2391–2403. doi:10.2514/1.41252

[3] Dragna, D., Cotté, B., Blanc-Benon, Ph., and Poisson, F., "Time-Domain Simulations of Outdoor Sound Propagation with Suitable Impedance Boundary Conditions," *AIAA Journal*, Vol. 49, No. 7, 2011, pp. 1420–1428. doi:10.2514/1.J050636

[4] Blumrich, R., and Heimann, D., "A Linearized Eulerian Sound Propagation Model for Studies of Complex Meteorological Effects," *Journal of the Acoustical Society of America*, Vol. 112, No. 2, 2002, pp. 446–455. doi:10.1121/1.1485971

[5] Dragna, D., Blanc-Benon, Ph., and Poisson, F., "Time-Domain Solver in Curvilinear Coordinates for Outdoor Sound Propagation over Complex Terrain," *Journal of the Acoustical Society of America*, Vol. 133, No. 6, 2013, pp. 3751–3763. doi:10.1121/1.4803863

[6] Bongini, E., Molla, S., Gautier, P. E., Habault, D., Mattéi, P. O., and Poisson, F., "Synthesis of Noise of Operating Vehicles: Development

Within SILENCE of a Tool with Listening Features," *Noise and Vibration Mitigation for Rail Transportation Systems*, Springer, Berlin–Heidelberg, 2008, pp. 320–326.

[7] Cotté, B., Blanc-Benon, Ph., Cremezi-Charlet, C., and Poisson, F., "High-Speed Train Noise Propagation at Mid-Ranges," *19th International Congress on Acoustics 2007*, Vol. 5, Curran Associates Inc., New York, 2007, pp. 2916–2921.

[8] Ostashev, V. E., Wilson, D. K., Liu, L., Aldridge, D. F., Symons, N. P., and Marlin, D. "Equations for Finite-Difference, Time-Domain Simulation of Sound Propagation in Moving Inhomogeneous Media and Numerical Implementation," *Journal of the Acoustical Society of America*, Vol. 117, No. 2, 2005, pp. 503–517. doi:10.1121/1.1841531

[9] Crighton, D. G., "Basic Principles of Aerodynamic Noise Generation," *Progress in Aerospace Sciences*, Vol. 16, No. 1, 1975, pp. 31–96. doi:10.1016/0376-0421(75)90010-X

[10] Dowling, A. P., and Ffowcs Williams, J. E., *Sound and Sources of Sound*, Ellis Horwood, New York, 1983, pp. 209–212.

[11] Leppington, F. G., and Levine, H., "The Sound Field of a Pulsating Sphere in Unsteady Rectilinear Motion," *Proceedings of the Royal Society of London*, Vol. A412, No. 1842, 1987, pp. 199–221. doi:10.1098/rspa.1987.0085

[12] Ochmann, M., "Exact Solutions for Sound Radiation from a Moving Monopole Above an Impedance Plane," *Journal of the Acoustical Society of America*, Vol. 133, No. 4, 2013, pp. 1911–1921. doi:10.1121/1.4794389

[13] Howe, M. S., *Acoustics of Fluid–Structure Interactions*, Cambridge Univ. Press, Cambridge, 1988, p. 46. doi:10.1017/CBO9780511662898

[14] Michalke, A., "A Note on Noncompact Acoustic Monopoles and Dipoles," *Journal of Sound and Vibration*, Vol. 117, No. 3, 1987, pp. 519–527. doi:10.1016/S0022-460X(87)80070-6

[15] Morse, P. M., and Ingard, K. U., *Theoretical Acoustics*, Princeton Univ. Press, Princeton, 1986, pp. 717–726.

[16] Roger, M., "Sound Radiation by Moving Surfaces and the Green's Functions Technique Theoretical Acoustics," *Noise Sources in Turbulent Shear Flows: Fundamentals and Applications*, edited by Camussi, R., Springer, New York, 2013, pp. 73–116. doi:10.1007/978-3-7091-1458-2_2

[17] Bogey, C., and Bailly, C., "A Family of Low Dispersive and Low Dissipative Explicit Schemes for Flow and Noise Computations," *Journal of Computational Physics*, Vol. 194, No. 1, 2004, pp. 194–214. doi:10.1016/j.jcp.2003.09.003

[18] Bogey, C., de Cacqueray, N., and Bailly, C., "A Shock-Capturing Methodology Based on Adaptative Spatial Filtering for High-Order Nonlinear Computations," *Journal of Computational Physics*, Vol. 228, No. 5, 2009, pp. 1447–1465. doi:10.1016/j.jcp.2008.10.042

[19] Berland, J., Bogey, C., Marsden, O., and Bailly, C., "High Order, Low Dispersive and Low Dissipative Explicit Schemes for Multiple-Scale and Boundary Problems," *Journal of Computational Physics*, Vol. 224, No. 2, 2007, pp. 637–662. doi:10.1016/j.jcp.2006.10.017

[20] Berland, J., Bogey, C., and Bailly, C., "Low-Dissipation and Low-Dispersion Fourth-Order Runge–Kutta Algorithm," *Computers and Fluids*, Vol. 35, No. 10, 2006, pp. 1459–1463. doi:10.1016/j.compfluid.2005.04.003

[21] Berenger, J. P., "A Perfectly Matched Layer for the Absorption of Electromagnetic Waves," *Journal of Computational Physics*, Vol. 114, No. 2, 1994, pp. 185–200. doi:10.1006/jcph.1994.1159

[22] Hornikx, M., Waxler, R., and Forssén, J., "The Extended Fourier Pseudospectral Time-Domain Method for Atmospheric Sound Propagation," *Journal of the Acoustical Society of America*, Vol. 128, No. 4, 2010, pp. 1632–1646. doi:10.1121/1.3474234

[23] Heng, C. C., "Propagation of Train Noise in Housing Estates," *Applied Acoustics*, Vol. 51, No. 1, 1997, pp. 1–12. doi:10.1016/S0003-682X(96)00055-2

[24] Kinsler, L. E., Frey, A. R., Coppens, A. B., and Sanders, J. V., *Fundamentals of Acoustics*, 4th ed., Wiley, New York, 2000, pp. 176–179.

[25] Norum, T. D., and Liu, C. H., "Point Source Moving Above a Finite Impedance Reflecting Plane: Experiment and Theory," *Journal of the Acoustical Society of America*, Vol. 63, No. 4, 1978, pp. 1069–1073. doi:10.1121/1.381839

[26] Li, K. M., Buret, M., and Attenborough, K., "The Propagation of Sound due to a Source Moving at High Speed in a Refracting Medium," *Euronoise 98. Designing for Silence. Prediction, Measurement and Evaluation of Noise and Vibrations*, edited by Fastl, H., and Scheuren, J., Vol. 2, German Acoustical Society, Berlin, 1998, pp. 955–960.

[27] Attenborough, K., Li, K. M., and Horoshenkov, K., *Predicting Outdoor Sound*, Taylor and Francis, Philadelphia, 2007, pp. 200–209.

[28] Reymen, Y., Baelmans, M., and Desmet, W., "Time-Domain Impedance Formulation Suited for Broadband Simulations," AIAA Paper 2007-3519, 2007.

[29] Miki, Y., "Acoustical Properties of Porous Materials: Modifications of Delany–Bazley Models," *Journal of the Acoustical Society of Japan*, Vol. 11, No. 1, 1990, pp. 19–24.

[30] Embleton, T. F. W., "Tutorial on Sound Propagation Outdoors," *Journal of the Acoustical Society of America*, Vol. 100, No. 1, 1996, pp. 31–48. doi:10.1121/1.415879

[31] Attenborough, K., "Acoustical Characteristics of Rigid Fibrous Absorbents and Granular Materials," *Journal of the Acoustical Society of America*, Vol. 73, No. 3, 1983, pp. 785–799. doi:10.1121/1.389045

[32] Attenborough, K., Bashir, I., and Taherzadeh, T. "Outdoor Ground Impedance Models," *Journal of the Acoustical Society of America*, Vol. 129, No. 5, 2011, pp. 2806–2819. doi:10.1121/1.3569740

A. Lyrintzis
Associate Editor